Design, Fabrication and Analysis of a Mach-Zehnder Interferometer

Alfia Naaz Shaikh

Pramatra Tech Services (India) Private Limited

Bangalore, India

Email: alfia@pramatra.in

Abstract—**This report details the design for a set of Mach-Zehnder Interferometer (MZI) circuits intended for fabrication on a $220\,\text{nm}$ silicon-on-insulator (SOI) platform using electron-beam lithography. The primary objective is to create structures that facilitate the accurate experimental extraction of the response of MZI compact models. One key parameter, the interferometer path length difference, is varied to target specific Free Spectral Ranges (FSRs). This report outlines the theoretical foundation of the MZI, details the simulation methodology, and provides an analysis of the results based on experimental observations.**

I. INTRODUCTION

A Mach-Zehnder Interferometer operates by splitting an input light beam into two separate paths, potentially introducing a relative phase shift between the paths, and then recombining the beams to produce interference. In its integrated form, an MZI typically comprises an input optical splitter (e.g., a Y-branch or directional coupler), two waveguide arms with lengths L_1 and L_2, and an output optical combiner. The key parameter for the unbalanced MZI considered here is the physical path length difference $\Delta L = L_2 - L_1$. This path length difference introduces a wavelength-dependent phase difference $\Delta\Phi$ between the light propagating through the two arms.

II. THEORY- MZI TRANSFER FUNCTION

Consider an ideal MZI with lossless waveguides and perfect 50:50 power splitters and combiners. Let the input electric field be E_{in}. After the input splitter, the field entering each arm is $E_{\text{in}}/\sqrt{2}$.

The light propagates through the arms, accumulating phase shifts $\phi_1 = \beta L_1$ and $\phi_2 = \beta L_2$, where β is the propagation constant of the guided mode, given by

$$\beta(\lambda) = \frac{2\pi n_{\text{eff}}(\lambda)}{\lambda}$$

Ignoring propagation loss, the fields arriving at the input ports of the combiner are,

$$E_1 = \frac{E_{\text{in}}}{\sqrt{2}} e^{-i\beta L_1}$$

and

$$E_2 = \frac{E_{\text{in}}}{\sqrt{2}} e^{-i\beta L_2}$$

At the output combiner (assuming a symmetric 50:50 device like a Y-branch), the fields from the two arms interfere. The combined field at the single output port, E_{out}, is proportional to the sum of the fields arriving from the two arms,

$$E_{\text{out}} = \frac{E_1 + E_2}{\sqrt{2}}$$

$$E_{\text{out}} = \frac{E_{\text{in}}}{2} (e^{-i\beta L_1} + e^{-i\beta L_2})$$

And the intensity is,

$$I_{\text{out}} = I_{\text{in}} \cos^2\left(\frac{\beta\Delta L}{2}\right)$$

III. MODELLING AND SIMULATION

A. Waveguide Characterization

The simulations are based on the standard Silicon-on-Insulator (SOI) platform, featuring a crystalline silicon (Si) core layer with a fixed height $h = 220$ nm, a top and a buried oxide (BOX) layer on a silicon substrate. The upper cladding is made of silicon dioxide. The default waveguide width is $w = 500$ nm.
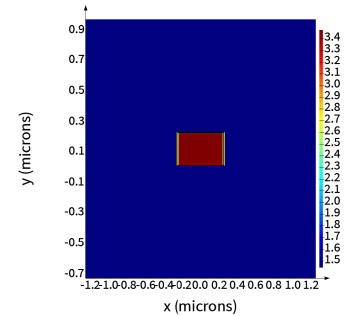

Fig. 1: Index profile of geometry

To study the mode profiles of the geometry, simulations are also performed using FDE MODE Solver from Ansys Lumerical. Simulations are conducted for the fundamental quasi-Transverse Electric (TE0) mode and the fundamental quasi-Transverse Magnetic (TM0) mode.

Consider the Taylor expansion around central wavelength, λ_0 for the effective index, n_{eff} as a function of wavelength,

$$n_{\text{eff}}(\lambda) = n_1 + n_2(\lambda - \lambda_0) + n_3(\lambda - \lambda_0)^2$$

where n_1, n_2, n_3, λ_0 are the parameters for the waveguide model. Running a frequency sweep over wavelength, a plot of
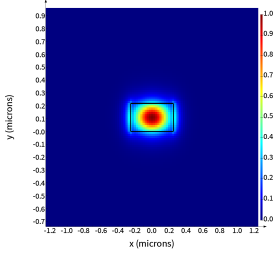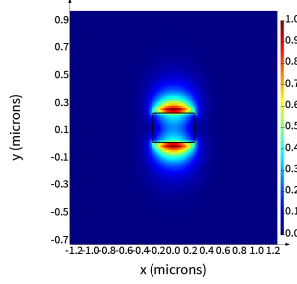
Fig. 2: TE polarization   Fig. 3: TM polarization

Fig. 4: Comparison of TE and TM polarization.

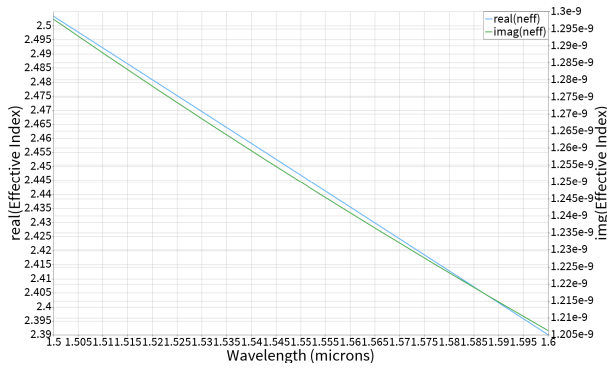effective index and group index of the waveguide is obtained with respect to wavelength.
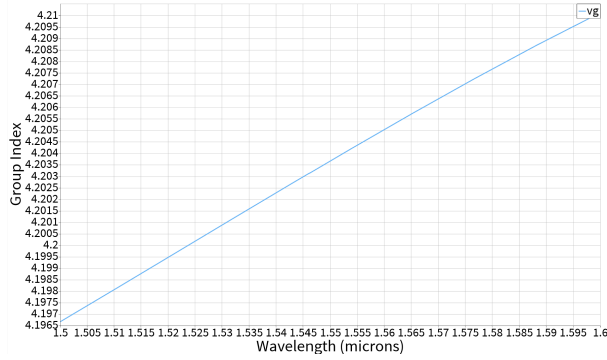

Fig. 5: Effective index variation

Fig. 6: Group index variation

B. Free Spectral Range (FSR)

The Free Spectral Range (FSR) is defined as the spacing in wavelength (or frequency) between adjacent transmission maxima (or minima) in the MZI spectrum. Therefore, the FSR for a MZI is given as,

$$\text{FSR} = \frac{\lambda^2}{n_g \Delta L}$$

This is the fundamental equation relating the measurable FSR to the group index n_g and the designed path length difference

ΔL at a given center wavelength λ. This derivation explicitly incorporates the group index, thereby accounting for the effect of waveguide dispersion on the FSR.

Experimentally, the FSR is measured from the transmission spectrum of the fabricated MZI at a specific center wavelength λ. The path length difference ΔL is a design parameter known from the device layout. Using these two values, the group index n_g at wavelength λ can be calculated. The simulation results of compact model for Mach-Zehnder with $\Delta L = 100$ μm are shown below:

TABLE I: Free Spectral Range (FSR) for different optical path length differences (ΔL)

ΔL (μm)	FSR (nm)
25	22.86
50	11.43
100	5.715
200	2.86
400	1.43

C. Photonic Circuit Transmission Spectrum

The transmission spectrum of the designed MZI circuit is simulated using Lumerical INTERCONNECT. This simulation provides the expected optical response of the device, which can then be compared with experimental measurements.
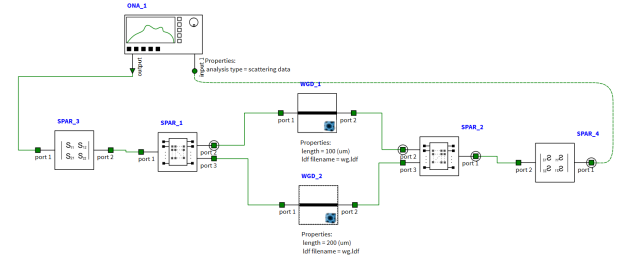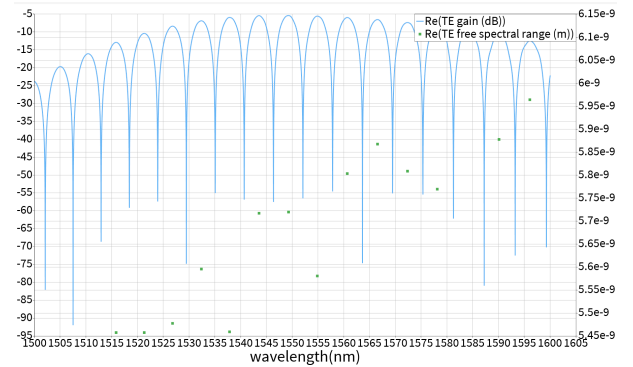

Fig. 7: Schematic of MZI compact mode

Fig. 8: Response of MZI

IV. FABRICATION- WASHINGTON NANOFABRICATION FACILITY (WNF) SILICON PHOTONICS PROCESS

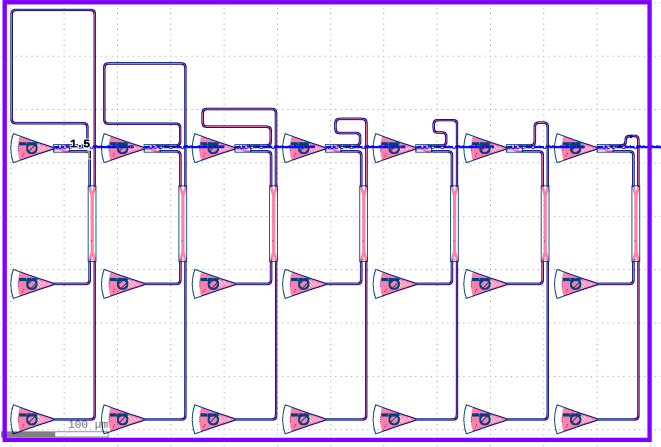The devices were fabricated using $100 \, \text{keV}$ electron beam lithography [1]. The fabrication used a silicon-on-insulator

Fig. 9: TE MZI Layout with variation in path length difference

(a) $\Delta L = 25\,\mu m$

(b) $\Delta L = 50\,\mu m$

(c) $\Delta L = 75\,\mu m$

(d) $\Delta L = 100\,\mu m$

(e) $\Delta L = 200\,\mu m$

(f) $\Delta L = 300\,\mu m$

(g) $\Delta L = 400\,\mu m$

Fig. 10: Simulation results for varying optical path length differences (ΔL).

wafer with a $220\,\mathrm{nm}$ thick silicon layer on a $3\,\mu m$ thick buried oxide. The substrates were $25\,\mathrm{mm}$ squares diced from $150\,\mathrm{mm}$ wafers. After a solvent rinse and a hot-plate dehydration bake, hydrogen silsesquioxane resist (HSQ, Dow-Corning XP-1541-006) was spin-coated at $4000\,\mathrm{rpm}$ and baked at $80\,^\circ\mathrm{C}$ for $4\,\mathrm{minutes}$.

Electron beam lithography was performed using a JEOL JBX-6300FS system operated at $100\,\mathrm{keV}$, with a beam current of $8\,\mathrm{nA}$ and an exposure field size of $500\,\mu m$. The machine grid for shape placement was $1\,\mathrm{nm}$, and the beam stepping grid (the spacing between dwell points) was $6\,\mathrm{nm}$. An exposure dose of $2800\,\mu\mathrm{C/cm^2}$ was used.

The resist was developed by immersion in $25\,\%$ tetramethylammonium hydroxide (TMAH) for $4\,\mathrm{minutes}$, followed by a deionized water rinse for $60\,\mathrm{s}$, an isopropanol rinse for $10\,\mathrm{s}$, and drying with nitrogen gas.

Unexposed silicon was etched using inductively coupled plasma (ICP) etching in an Oxford Plasmalab System 100. The process used a chlorine gas flow of $20\,\mathrm{sccm}$, pressure of $12\,\mathrm{mTorr}$, ICP power of $800\,\mathrm{W}$, RF bias power of $40\,\mathrm{W}$, and platen temperature of $20\,^\circ\mathrm{C}$, resulting in a bias voltage of $185\,\mathrm{V}$. During etching, chips were mounted on a $100\,\mathrm{mm}$ silicon carrier wafer using perfluoropolyether (PFPE) vacuum oil.

Cladding oxide was deposited using plasma-enhanced chemical vapor deposition (PECVD) in the same Oxford Plasmalab System 100. Process parameters included a silane (SiH_4) flow of $13.0\,\mathrm{sccm}$, nitrous oxide (N_2O) flow of $1000.0\,\mathrm{sccm}$, nitrogen (N_2) flow of $500.0\,\mathrm{sccm}$, chamber pressure of $1400\,\mathrm{mTorr}$, high-frequency RF power of $120\,\mathrm{W}$, and platen temperature of $350\,^\circ\mathrm{C}$. During deposition, the chips were placed directly on a silicon carrier wafer and buffered on all sides by silicon pieces to improve uniformity.

V. EXPERIMENT DATA

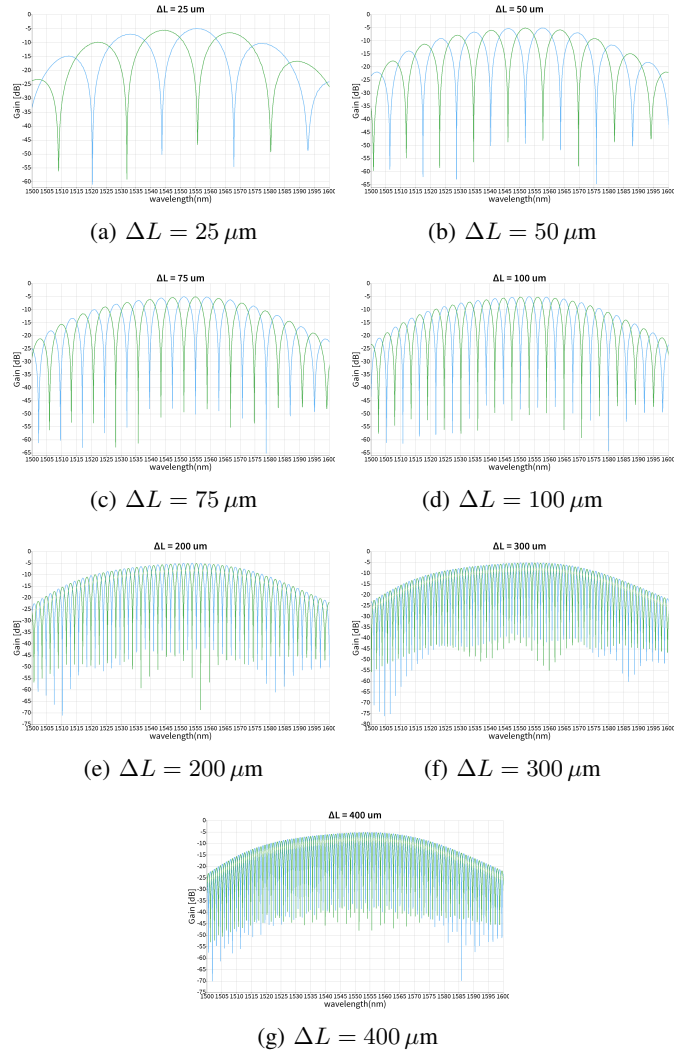To characterize the devices, a custom-built automated test setup [2], [3] with automated control software written in Python was used [3]. An Agilent 81600B tunable laser was used as the input source and Agilent 81635A optical power sensors as the output detectors. The wavelength was swept from 1500 to 1600 nm in 10 pm steps. A polarization-maintaining (PM) fibre was used to maintain the polarization state of the light, to couple the TE polarization into the grating couplers [4]. A 90° rotation was used to inject light into the TM grating couplers [4]. A polarization-maintaining fibre array was used to couple light in/out of the chip [5].

VI. ANALYSIS

A. Monte Carlo Simulation

To gain a more comprehensive statistical understanding of the impact of manufacturing variations, Monte Carlo simulations were performed. This approach involves randomly sampling waveguide parameters (e.g., width and height) within their defined statistical distributions (e.g., Gaussian distribution with a specified mean and standard deviation) and then simulating the device performance for each sample. This pro-
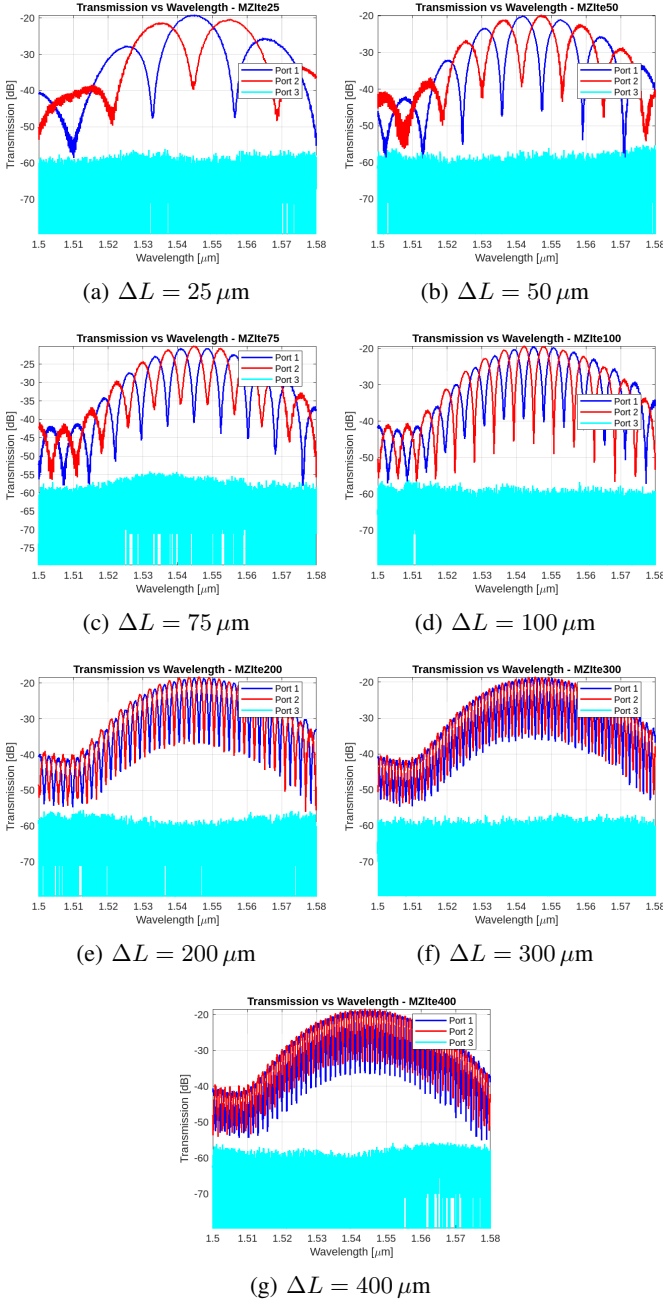
(a) $\Delta L = 25\,\mu\text{m}$

(b) $\Delta L = 50\,\mu\text{m}$

(c) $\Delta L = 75\,\mu\text{m}$

(d) $\Delta L = 100\,\mu\text{m}$

(e) $\Delta L = 200\,\mu\text{m}$

(f) $\Delta L = 300\,\mu\text{m}$

(g) $\Delta L = 400\,\mu\text{m}$

Fig. 11: Experimental results for varying optical path length differences (ΔL).

found to be $5.77\,\text{nm}$ with a standard deviation of $0.155\,\text{nm}$ for a specific MZI design.
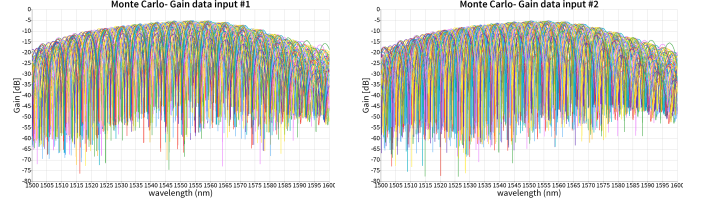
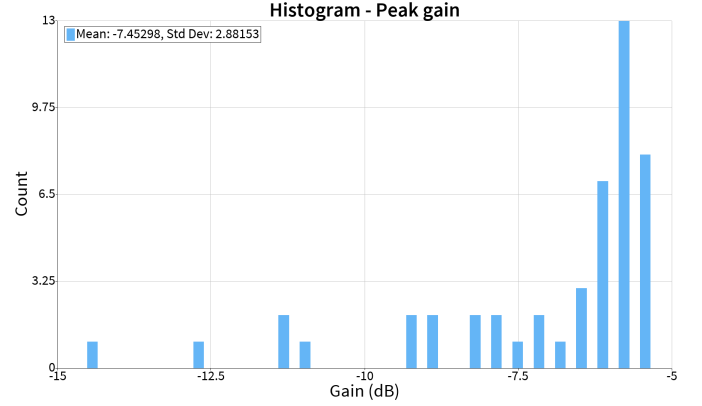
Fig. 12: Monte Carlo- Gain1

Fig. 13: Monte Carlo- Gain2
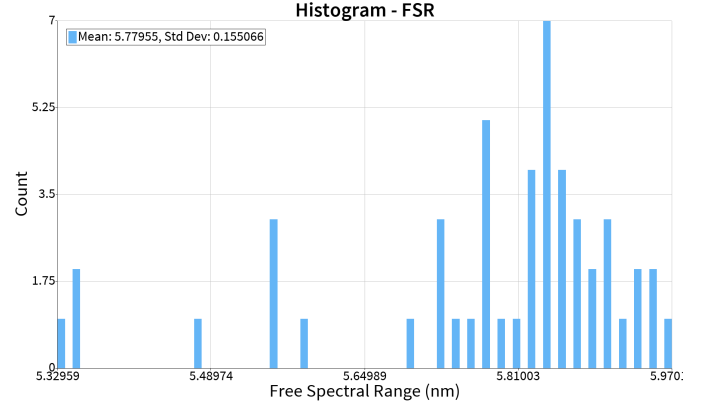

Fig. 14: Histogram-gain

Fig. 15: Histogram-fsr

cess was executed directly from the KLayout layout using the integrated compact models for Lumerical INTERCONNECT.

The simulation results provide histograms for key device and circuit parameters, such as waveguide effective index (n_{eff}), group index (n_g), and MZI FSR. These histograms visually represent the distribution of these parameters across 50 fabrication runs on the same wafer. By inspecting the mean and standard deviation values of these distributions, we can quantify the expected variability and assess the manufacturing yield of the designed devices. For instance, the mean FSR was

B. Corner Analysis

Manufacturing challenges, particularly variations in waveguide dimensions (height and width), can significantly impact the optical properties of integrated photonic devices. To understand and quantify this impact, a corner analysis was performed. This analysis involves simulating the waveguide and MZI performance at the extreme limits of expected fabrication tolerances for width (w) and height (h). Specifically, four corners were considered:

- Nominal: $w = 500\,\text{nm}$, $h = 220\,\text{nm}$
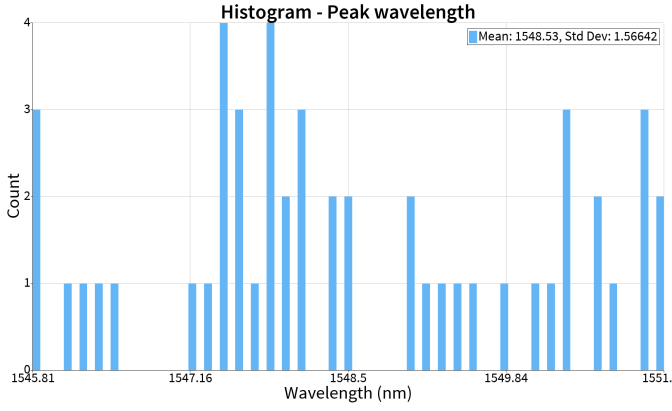- Corner 1 (Min Width, Max Height): $w = w_{\text{min}}$, $h = h_{\text{max}}$

Fig. 16: Histogram-wvl

- Corner 2 (Max Width, Min Height): $w = w_{\max}$, $h = h_{\min}$
- Corner 3 (Min Width, Min Height): $w = w_{\min}$, $h = h_{\min}$
- Corner 4 (Max Width, Max Height): $w = w_{\max}$, $h = h_{\max}$

For each corner, the waveguide effective index (n_{eff}) and group index (n_g) were simulated across the wavelength range of interest. The results, as shown in Figure 17 and Figure 18, indicate that variations in waveguide dimensions lead to noticeable shifts in both n_{eff} and n_g curves.

The impact on the MZI's Free Spectral Range (FSR) was also determined for each corner. Since FSR is inversely proportional to $n_g \Delta L$, changes in n_g directly translate to variations in FSR. Table II summarizes the FSR values obtained for a specific ΔL (e.g., $100 \, \mu\text{m}$) at each corner. These results highlight the range of FSR values that can be expected from fabricated devices due to manufacturing tolerances.
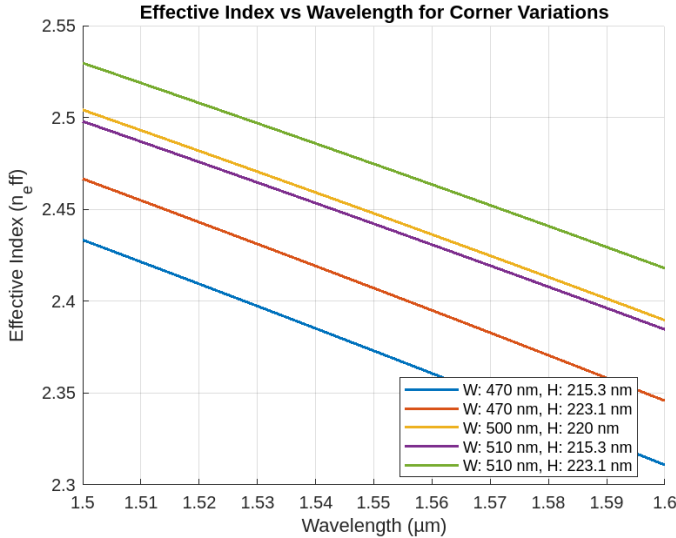

Fig. 17: Effective Index variation for Corner Analysis

VII. CONCLUSION

This report has detailed the comprehensive design, simulation, and initial characterization of Mach-Zehnder Interferometer (MZI) circuits on a $220 \, \text{nm}$ silicon-on-insulator
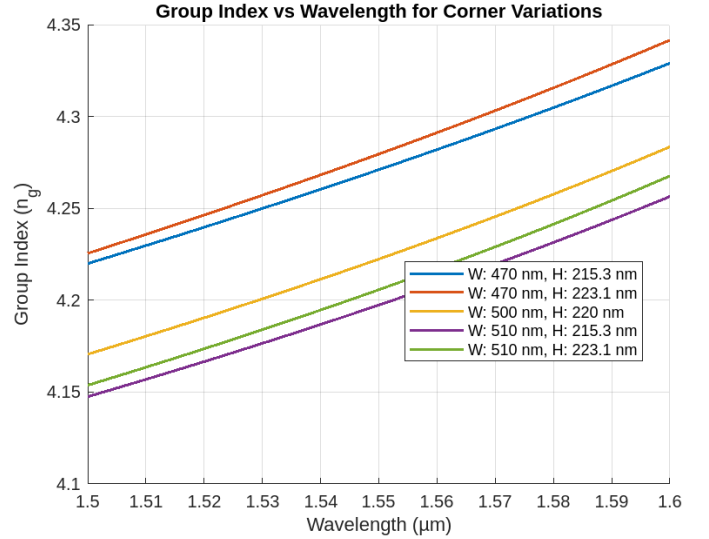

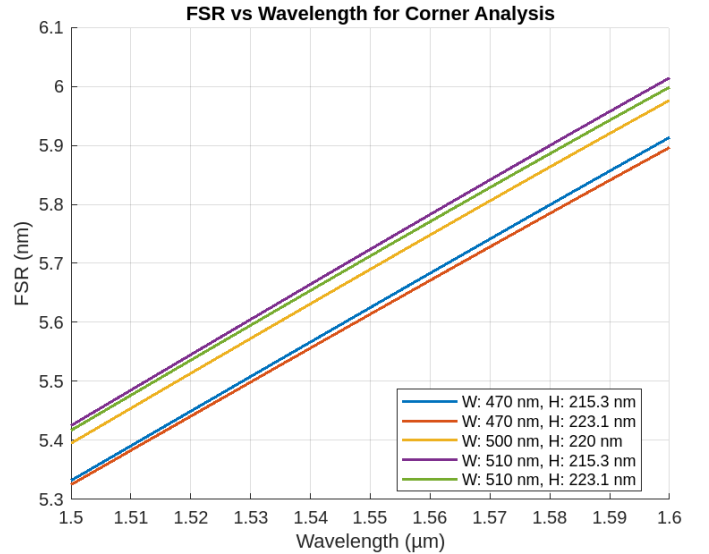Fig. 18: Group Index variation for Corner Analysis

Fig. 19: Free Spectral Range variation for Corner Analysis

TABLE II: Impact of Corner Analysis on FSR for $\Delta L = 100 \, \mu\text{m}$

Waveguide Parameters	Value (nm)	FSR (nm)
Minimum Width, Minimum Height	470, 215.3	5.618
Minimum Width, Maximum Height	470, 223.1	5.607
Nominal	500, 220	5.6825
Maximum Width, Minimum Height	500, 215.3	5.716
Maximum Width, Maximum Height	500, 223.1	5.705

(SOI) platform. The primary objective of enabling accurate experimental extraction of MZI compact model responses, particularly the waveguide group index, was addressed through a systematic approach.

The theoretical framework for the MZI transfer function was established, providing the foundation for the compact modeling. Waveguide characterization, including mode profile
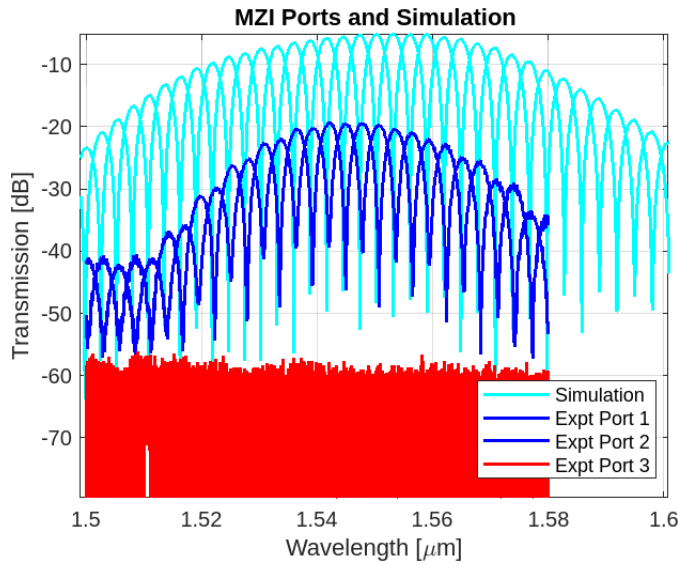
Fig. 20: MZI spectrum or path length difference of 100 μ m

analysis and the development of a polynomial compact model for the effective index, demonstrated the fundamental optical properties of the designed structures. The derivation of the group index from the MZI's Free Spectral Range (FSR) proved crucial for both simulation-based prediction and experimental extraction.

Crucially, the impact of manufacturing challenges was thoroughly investigated. Corner analysis provided insight into the sensitivity of key device parameters, such as effective index, group index, and FSR, to anticipated fabrication variations in waveguide width and height. Furthermore, Monte Carlo simulations offered a statistical understanding of device performance variability, highlighting the expected distributions and enabling a quantitative assessment of design robustness against random process fluctuations. The methodologies presented are instrumental for developing accurate compact models, predicting the impact of manufacturing variations, and extracting critical waveguide parameters from experimental data, thereby advancing the development of reliable and high-performance integrated photonic circuits. Future work will focus on refining the compact models with more extensive experimental data, exploring advanced fitting algorithms, and extending the analysis to more complex photonic integrated circuits.

ACKNOWLEDGMENT

REFERENCES

[1] R. J. Bojko, J. Li, L. He, T. Baehr-Jones, M. Hochberg, and Y. Aida, "Electron beam lithography writing strategies for low loss, high confinement silicon optical waveguides," *Journal of Vacuum Science & Technology B*, vol. 29, no. 6, 2011.

[2] PLC Connections, "PLC Connections Website." http://www.plcconnections.com, 2025. Accessed: July 8, 2025.

[3] M. Caverley, "SiEPIC Probe Station." http://siepic.ubc.ca/probestation. Python code developed by Michael Caverley; Accessed: July 8, 2025.

[4] L. Chrostowski and M. Hochberg, *Silicon photonics design: from devices to systems*. Cambridge University Press, 2015.

[5] Maple Leaf Photonics, "Maple Leaf Photonics Website." http://mapleleafphotonics.com, 2025. Accessed: July 8, 2025.